

Cohesive modeling of dewetting in particulate composites: micromechanics vs. multiscale finite element analysis

H.M. Inglis^a, P.H. Geubelle^{b,*}, K. Matouš^{b,c}, H. Tan^a, Y. Huang^a

^a *Department of Mechanical Science and Engineering, University of Illinois at Urbana-Champaign, 1206 W. Green Street, Urbana, IL 61801, USA*

^b *Department of Aerospace Engineering, University of Illinois at Urbana-Champaign, 104 South Wright Street, Urbana, IL 61801, USA*

^c *Center for Simulation of Advanced Rockets, University of Illinois at Urbana-Champaign, 1304 West Springfield Avenue, Urbana, IL 61801, USA*

Received 23 December 2005

Abstract

The effect of damage due to particle debonding on the constitutive response of highly filled composites is investigated using two multiscale homogenization schemes: one based on a closed-form micromechanics solution, and the other on the finite element implementation of the mathematical theory of homogenization. In both cases, the particle debonding process is modeled using a bilinear cohesive law which relates cohesive tractions to displacement jumps along the particle–matrix interface. The analysis is performed in plane strain with linear kinematics. A detailed comparative assessment between the two homogenization schemes is presented, with emphasis on the effect of volume fraction, particle size and particle-to-particle interaction.

© 2006 Elsevier Ltd. All rights reserved.

Keywords: Particle-reinforced composites; Debonding; Microstructure; Damage mechanics; Micromechanics; Homogenization

1. Introduction

This paper focuses on the modeling of particle debonding (sometimes referred to as *dewetting*) in particulate composites, with special emphasis on systems characterized by high reinforcement volume fraction and substantial modulus mismatch between constituents. Examples include solid propellants (SP), energetic materials and other reinforced elastomers, which are typically composed of stiff

particles (such as ammonium perchlorate and aluminum for SP) bonded together in a very compliant elastomeric matrix. The particles in these materials range from a few micrometers to several hundred micrometers in diameter, with a total volume fraction as high as 75%.

Bencher et al. (1995) and Ide and Ho (1999) have studied fracture processes in solid propellants at low strain rates ($\sim 10^{-3} \text{ s}^{-1}$) and temperatures ranging from -55 to 70 °C. They report a damage process which begins with particle dewetting and formation of matrix fibrils ahead of the crack tip followed by void coalescence and fibril rupture leading to crack advancement. Temperature decrease results in

* Corresponding author.

E-mail address: geubelle@uiuc.edu (P.H. Geubelle).

strengthening of the elastomeric matrix and increased occurrence of particle debonding rather than matrix tearing, leading to an increase in the size of the process zone and higher fracture toughness.

In experiments on an inert comparison material, [Trumel et al. \(2001\)](#) also noted particle debonding as the origin of the damage process in uniaxial quasi-static tests. This is in contrast to the behavior under high strain rates (10^3 s^{-1}), in which particle fracture is the dominant failure mode, and high pressures ($\sim 500 \text{ MPa}$), in which grain plasticity is observed. [Rae et al. \(2002a,b\)](#) performed experiments on high explosive, another closely packed particulate composite system. Their results show clearly that the damage process is dominated by failure of the particle–matrix interface, with failure initiating at multiple sites perpendicular to the applied loading direction, especially along the boundaries of large particles.

Failure in energetic materials is thus dominated by processes which occur at a scale of several hundred microns, orders of magnitude smaller than the scales of the structural components in which they are commonly used. It is prohibitively expensive to model a typical component with sufficient resolution to capture the failure processes, hence it is customary to model different scales separately and introduce simplifying assumptions to bridge them. The most common assumption is that it is possible to represent the complexity of the microstructure through some average material characterization at the macroscale, a process of “smearing” or homogenization of the microstructural response. We consider hereafter two complementary homogenization approaches—an analytical method based on micromechanics, and a numerical scheme based on the mathematical theory of homogenization (MTH).

Micromechanics relates microstructural phenomena such as heterogeneities to the mechanics of material behavior. Building on Eshelby’s detailed analytical solution of the problem of an ellipsoidal inclusion in an infinite matrix ([Eshelby, 1957](#)), the method is extended by considering boundary conditions which account for some interactions between particles. In the Mori–Tanaka method ([Mori and Tanaka, 1973](#)), the inclusion is subjected to the local strain in the surrounding matrix, while the self-consistent method, attributed to [Hill \(1965\)](#) and [Budiansky \(1965\)](#), embeds the particle in a material with the properties of the homogenized composite.

The Hashin–Shtrikman bounds ([Hashin and Shtrikman, 1962](#)) are computed by comparing the composite to a reference material, with stiffness either greater than any element in the composite (upper bound) or less than every element (lower bound). Similar bounds on material properties are obtained numerically by imposing either traction or displacement on the boundaries of a representative volume element (RVE). In recent work, [Kanit et al. \(2003\)](#) compare such results to those obtained when the unit cell is assumed to be the base cell of a periodic microstructure and periodic boundary conditions are imposed.

Homogenization methods based on asymptotic expansions of solution fields were presented by [Bensoussan et al. \(1978\)](#) and [Sanchez-Palencia \(1980\)](#) to study periodic heterogeneous media. As outlined by [Guedes and Kikuchi \(1990\)](#), the mathematical theory of homogenization (MTH) provides a powerful framework for linking multiple length scales, well suited to computation. This approach has been used extensively by various research groups; see, for example, [Ghosh et al. \(1995\)](#); [Raghavan et al. \(2001\)](#); [Fish et al. \(1997\)](#).

When an analytical solution is available, a micromechanics model is substantially cheaper than a numerical solution. However, the assumptions required for an analytical solution to be tractable tend to reduce the accuracy of the model. In this work, we are interested in evaluating the extent to which the simplified model still provides valid material representation, or, at the least, useful physical insights in the case of particle dewetting.

The micromechanics model can be validated through comparison with experimental results. However, when the analytical and empirical results differ, to what do we attribute the error? The error may be a consequence of material assumptions (i.e., linear elasticity, small strain) or of simplifications used to arrive at the micromechanics model (i.e., spherical particles, hydrostatic stress, uniform fields in phases). Often, due to the limitations of experimentation, only a single macroscopic comparison can be made quantitatively, while microscopic comparison is qualitative at best. Hence comparison with experimental data is not always sufficient to identify errors in the model and consequently improve it. There is a role for solution verification by comparison with a reference numerical solution. In this paper, we therefore perform such a comparison between a micromechanics model and a numerical MTH scheme that incorporates the same

material and failure models, but accounts for heterogeneous fields and particle interactions and allows for complex loading paths.

The micromechanics model follows that used by Tan et al. (2005a, 2006) to investigate the debonding of spherical particles under remote hydrostatic tension. Debonding at the particle–matrix interface was modeled through the use of a bilinear cohesive law. Beginning with a dilute homogenization assumption (Tan et al., 2006), the model was subsequently extended to a Mori–Tanaka homogenization procedure (Tan et al., 2005a), which is valid for a larger range of volume fractions. Although based on highly simplifying assumptions (linear kinematics and material response), the micromechanics models captured the size effect observed experimentally, with large particles debonding before small particles. The authors identified a critical particle radius a_{cr} above which the composite softens rather than hardens after debonding, causing the interface to undergo continuous debonding even under static load.

The other homogenization approach considered in this paper, the MTH-based finite element scheme, served as the foundation of the analysis performed by Matouš and Geubelle (2006) in a finite strain setting with cohesive zone modelling of interface failure. The finite element formulation was stabilized to handle the near-incompressible behavior of the matrix. Simulations of one- and four-particle unit cells of an idealized solid propellant allowed microscale failure processes to be linked with macroscopic stress–strain curves, including an example in which load path bifurcation occurs. The results presented in Matouš and Geubelle (2006) are not predictive, as the size and simplicity of the unit cell adopted in that study do not approach the statistical representativity required of an RVE except for very organized microstructures. Increasing problem size would substantially increase the computational costs. In order to further study the physics of particle debonding in closely packed materials with much larger unit cells, a simpler computational model, based on assumptions of linear kinematics and plane strain, is developed in this paper. This simpler model provides a useful tool for investigation of multiple physical phenomena, while not attempting to approach the accuracy of the above work.

The objective of this paper is thus to perform a detailed comparative study between these two modeling approaches to assess the range of validity of

the micromechanics model in the cohesive modeling of dewetting in particulate composites. As it was the case in the micromechanics study, this comparative analysis relies on linear kinematics (small strain), linear elasticity and equibiaxial loading assumptions, although the numerical homogenization scheme can readily incorporate finite kinematics, nonlinear material response and more complex loading cases (Matouš and Geubelle, 2006). The comparison is performed under the plane strain assumption, in which the inclusions are actually fibers rather than spheres, although we will continue to refer to “particles” and “particulate composites”. Both approaches use identical constitutive models for the constituents and their interface.

Section 2 sets out the general problem to be solved, and defines the cohesive law and material properties which will be used. In Section 3, we develop the plane strain version of the micromechanics model introduced by Tan et al. (2005a, 2006) and present the key results of this homogenization scheme. Section 4 is devoted to the presentation, implementation and application of the MTH-based finite element method. Simulated damage evolutions obtained on a variety of loading conditions and their effect on the macroscopic constitutive response of the composite are also presented. However, the comparison between these two homogenization schemes, discussed in Section 5, is limited to the equibiaxial loading case. In Section 6, we evaluate the performance of the micromechanics model, and present conclusions.

2. Problem description

The problem of interest consists of a heterogeneous material composed of particles Ω^{p_I} embedded in a matrix Ω^m and subjected to a macroscopic stress $\bar{\sigma}$ or strain $\bar{\epsilon}$. The volume fraction of particle I is given by $f_I = \Omega^{p_I} / \Omega$, satisfying $\sum_I f_I = f$. Superscripts m , p_I and int denote the matrix, particle I and interface, respectively. The composite experiences damage through debonding of the particle–matrix interface, denoted S^{p_I} . We aim to determine the macroscopic stress–strain response of the composite during damage evolution.

The debonding of the particle from the surrounding matrix is modeled through a traction–separation law at the cohesive interface. Tan et al. (2005b) present experimental results justifying the use of a bilinear cohesive law, specified in terms of interface properties,

$$\sigma^{\text{int}} = \begin{cases} k_{\sigma} \llbracket u_r \rrbracket & \text{for } \llbracket u_r \rrbracket \leq \frac{\sigma_{\text{max}}}{k_{\sigma}}, \\ \left(1 + \frac{\tilde{k}_{\sigma}}{k_{\sigma}}\right) \sigma_{\text{max}} - \tilde{k}_{\sigma} \llbracket u_r \rrbracket & \text{for } \frac{\sigma_{\text{max}}}{k_{\sigma}} \llbracket u_r \rrbracket < \sigma_{\text{max}} \left(\frac{1}{k_{\sigma}} + \frac{1}{\tilde{k}_{\sigma}}\right), \\ 0 & \text{for } \llbracket u_r \rrbracket > \sigma_{\text{max}} \left(\frac{1}{k_{\sigma}} + \frac{1}{\tilde{k}_{\sigma}}\right) \end{cases} \quad (1)$$

where σ_{max} , k_{σ} and \tilde{k}_{σ} respectively represent the interface strength, modulus and softening modulus of the interface, and $\llbracket u_r \rrbracket$ is the interface opening (or displacement jump) in the radial direction, making use of the discontinuity notation $\llbracket \bullet \rrbracket$. Since the loading condition is hydrostatic, they consider only normal extension and do not account for tangential opening or for normal compression.

The bilinear irreversible cohesive law used in the numerical simulations presented in Section 4 is that described by Geubelle and Baylor (1998), which, at each point along the interface, relates the normal (T_n) and tangential (T_t) cohesive tractions to the normal (Δn) and tangential (Δt) displacement jumps through

$$T_n = \begin{cases} \frac{\sigma_{\text{max}}}{S_{\text{init}}} \frac{S}{1-S} \frac{\Delta n}{\Delta n_c} & \text{for } \Delta n \geq 0, \\ \frac{\sigma_{\text{max}}}{1-S_{\text{init}}} \frac{\Delta n}{\Delta n_c} & \text{for } \Delta n < 0, \end{cases} \quad (2)$$

$$T_t = \frac{\tau_{\text{max}}}{S_{\text{init}}} \frac{S}{1-S} \frac{\Delta t}{\Delta t_c}. \quad (3)$$

The coupling between normal and tangential failure is achieved through an interface damage parameter S , which degrades from its initial value S_{init} , chosen close to unity, to 0 with increased interface opening according to

$$S = \langle\langle 1 - \|\tilde{\Delta}\|_2 \rangle\rangle = \left\langle\left\langle 1 - \sqrt{\left(\frac{\Delta n}{\Delta n_c}\right)^2 + \left(\frac{\Delta t}{\Delta t_c}\right)^2} \right\rangle\right\rangle \quad (4)$$

when Δn is positive. In the case of compression ($\Delta n < 0$), no further accumulation of damage is allowed. In the above expression, $\langle\langle a \rangle\rangle = a$ if $a > 0$ and $\langle\langle a \rangle\rangle = 0$ otherwise. S represents the remaining capacity of the local interface to sustain tractions. The parameters σ_{max} and τ_{max} entering (2) and (3) denote the tensile and shear interface strengths respectively, while Δn_c and Δt_c represent the critical normal and tangential values of the opening displacements beyond which complete failure is assumed.

As shown in Fig. 1, the cohesive laws used in the micromechanics model and in the numerical simulations are identical for the normal opening direction in the absence of shear failure, when cohesive stiffnesses are related through

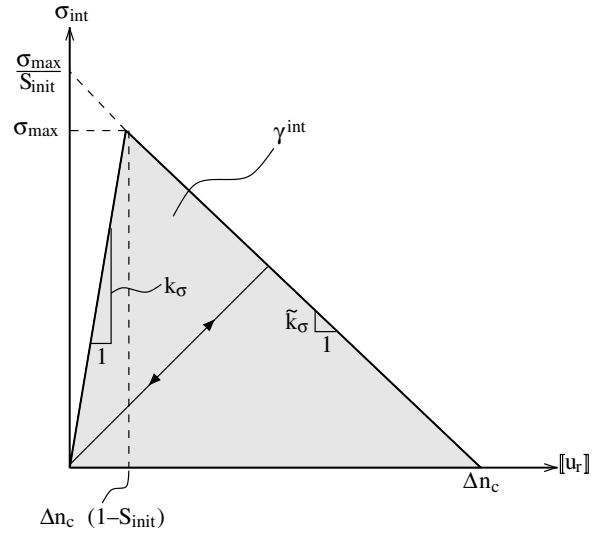


Fig. 1. Bilinear cohesive law for opening in the normal direction. The unloading path is always directed towards the origin.

$$k_{\sigma} = \frac{\sigma_{\text{max}}}{(1 - S_{\text{init}}) \Delta n_c}, \quad (5)$$

$$\tilde{k}_{\sigma} = \frac{\sigma_{\text{max}}}{S_{\text{init}} \Delta n_c}, \quad (6)$$

and the interface fracture toughness, (i.e., the area under the traction-separation curve) is given by

$$\gamma^{\text{int}} = \frac{\sigma_{\text{max}}^2}{2} \left(\frac{1}{k_{\sigma}} + \frac{1}{\tilde{k}_{\sigma}}\right) = \frac{1}{2} \sigma_{\text{max}} \Delta n_c. \quad (7)$$

The interface properties, given in Table 1, and volumetric material properties, given in Table 2, have been chosen to ensure that failure occurs within the limit of small strain, as the linear kinematics assumption is invoked in both the micromechanics and MTH models. This is acceptable, since we are

Table 1
Cohesive interface properties

Property	Symbol	Value
<i>Interface strength (MPa)</i>		
Normal	σ_{max}	0.02
Tangential	τ_{max}	0.02
<i>Critical opening displacement (μm)</i>		
Normal	Δn_c	1.0
Tangential	Δt_c	1.0
<i>Linear modulus (MPa/μm)</i>		
Softening modulus (MPa/ μm)	\tilde{k}_{σ}	0.02
Initial damage (-)	S_{init}	0.98
Interface energy (MPa μm)	γ^{int}	0.01

Table 2
Volumetric material properties

Constituent	E (MPa)	ν
Particles	150	0.3
Binder	1	0.4

interested in comparing two models using identical material properties. Throughout the paper, all results are normalized with respect to the chosen properties. Note the large mismatch between the material properties of the matrix and the particles.

3. Micromechanics model

The micromechanics model with debonding presented by Tan et al. (2005a, 2006) is reformulated here for plane strain conditions. Only the key plane strain results are summarized hereafter: for more detail, the reader is referred to the above references. In this section and the remainder of this paper, uppercase subscripts denote the particle number and are not summed over unless explicitly specified, while lowercase indices follow conventional summation rules and in this plane strain setting take the values 1 and 2.

To find a relationship between macroscopic strain, $\bar{\epsilon}$, and macroscopic stress, $\bar{\sigma}$, we begin with the following expression for the macroscopic strain taken from Benveniste and Aboudi (1984):

$$\bar{\epsilon} = \mathbf{M}^m : \bar{\sigma} + \sum_I f_I \{ (\mathbf{M}^{pI} - \mathbf{M}^m) : \langle \boldsymbol{\sigma}^p \rangle_I + \langle \boldsymbol{\epsilon}^{\text{int}} \rangle_I \}, \quad (8)$$

where \mathbf{M} is the material compliance tensor, $\langle \boldsymbol{\sigma}^p \rangle_I$ represents the stress average over particle I , and $\langle \boldsymbol{\epsilon}^{\text{int}} \rangle_I$ represents the strain average over interfaces around particle I ,

$$\langle \boldsymbol{\epsilon}^{\text{int}} \rangle_I = \frac{1}{2\Omega^{pI}} \int_{S^{pI}} (\llbracket \mathbf{u} \rrbracket \otimes \mathbf{n} + \mathbf{n} \otimes \llbracket \mathbf{u} \rrbracket) dA, \quad (9)$$

where \mathbf{n} is the normal to the cohesive interface. In other words, the macroscopic (or average) strain can be considered as the strain due to the average stress applied to the matrix material, with perturbations due to the stress in each particle and due to the displacement discontinuity at the damaged particle–matrix interfaces. Note that this relation is general and only assumes linearity of the matrix and particle constitutive laws.

In order to find the macroscopic stress–strain relationship, we need to investigate the stress within

particles and the strain across particle interfaces. We make simplifying assumptions in order to proceed with an analytical solution: isotropy of particles and matrix, equibiaxial applied strain $\bar{\epsilon}$ and cylindrical particles of radius a_I . These assumptions reduce the problem to an axisymmetric one and ensure uniform stress fields in the particles. The average stress in a particle is then given by

$$\frac{1}{2} \langle \boldsymbol{\sigma}_{kk}^p \rangle_I = \sigma_I^{\text{int}}, \quad (10)$$

while the interface strain (9) reduces to

$$\langle \boldsymbol{\epsilon}_{kk}^{\text{int}} \rangle_I = \frac{2 \langle \llbracket u_r \rrbracket \rangle_I}{a_I}. \quad (11)$$

The relationship between interface traction and displacement jump is the cohesive interface law (1). The relationship between displacement jump and macroscopic stress requires a further assumption about the stress in the matrix surrounding the particle. The dilute assumption considers the particle to be embedded in an infinite matrix subjected to remote equibiaxial stress $\bar{\sigma}$. The Mori–Tanaka assumption, by contrast, considers a particle embedded in the local matrix and subjected to stress $\boldsymbol{\sigma}^m$, with the macroscopic stress balanced by

$$\bar{\sigma} = (1 - f) \boldsymbol{\sigma}^m + \sum_I f_I \langle \boldsymbol{\sigma}^p \rangle_I. \quad (12)$$

It is clear that, for small f , the Mori–Tanaka and the dilute assumptions converge, as we would expect. The two assumptions are represented schematically in Fig. 2.

The displacement discontinuity is readily determined (Timoshenko and Goodier, 1970) to be

$$\llbracket u_r \rrbracket = a_I \left[\frac{2(1 - \nu^m)(1 + \nu^m) \sigma^E - (1 + \nu^m) \sigma^{\text{int}}}{E^m} - \frac{\sigma^{\text{int}}}{2K_{\text{pl}-\epsilon}^{pI}} \right], \quad (13)$$

where $K_{\text{pl}-\epsilon}$ is the plane strain bulk modulus expressed in terms of the Young's modulus E and Poisson's ratio ν as

$$K_{\text{pl}-\epsilon} = \frac{E}{2(1 - 2\nu)(1 + \nu)}, \quad (14)$$

and σ^E denotes the macroscopic applied equibiaxial stress,

$$\sigma^E = \begin{cases} \bar{\sigma}, & \text{for the dilute model,} \\ \boldsymbol{\sigma}^m, & \text{for the Mori–Tanaka model.} \end{cases}$$

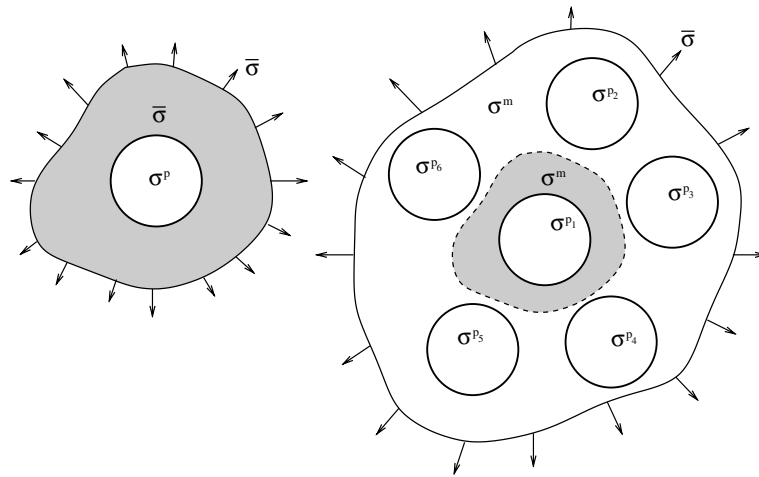


Fig. 2. Schematic comparison of dilute (left) and Mori–Tanaka (right) assumptions under conditions of remote equibiaxial stress.

We use (13) to rewrite the cohesive law (1) as

$$\sigma^{\text{int}} = \begin{cases} \alpha_I \sigma^E, & \text{undamaged} \\ \left(1 + \frac{\alpha'_I}{\alpha_I}\right) \sigma_{\text{max}} - \alpha'_I \sigma^E, & \text{transition} \\ 0, & \text{fully damaged} \end{cases} \quad (15)$$

where α_I and α'_I are functions of the material properties:

$$\alpha_I = \frac{2(1 - \nu^m)(1 + \nu^m)}{\frac{E^m}{k_\sigma a_I} + \frac{E^m}{2K_{\text{pl}}^m} + 1 + \nu^m}, \quad (16)$$

$$\alpha'_I = -\frac{2(1 - \nu^m)(1 + \nu^m)}{-\frac{E^m}{k_\sigma a_I} + \frac{E^m}{2K_{\text{pl}}^m} + 1 + \nu^m}. \quad (17)$$

The macroscopic strain in the composite can now be found by substituting (10) through (13) in (8) for the dilute and Mori–Tanaka cases, respectively:

$$\bar{\epsilon}^D = \frac{2(1 + \nu^m)(1 - \nu^m)}{E^m} \left[\left(\frac{1 - 2\nu^m}{2(1 - \nu^m)} + f \right) \bar{\sigma} - \sum_I f_I \sigma_I^{\text{int}} \right], \quad (18)$$

$$\bar{\epsilon}^{\text{MT}} = \frac{2(1 + \nu^m)(1 - \nu^m)}{E^m(1 - f)} \left[\frac{1 - 2\nu^m + f}{2(1 - \nu^m)} \bar{\sigma} - \sum_I f_I \sigma_I^{\text{int}} \right], \quad (19)$$

where σ_I^{int} is related to $\bar{\sigma}$ through (15). The dilute and Mori–Tanaka macroscopic stress–strain curves obtained for the volumetric and cohesive properties described in Section 2 and for a relatively small volume fraction ($f = 0.2$) of 40 μm radius particles are shown in Fig. 3. For a single particle size ($I = 1$) and the equibiaxial loading case, the constitutive re-

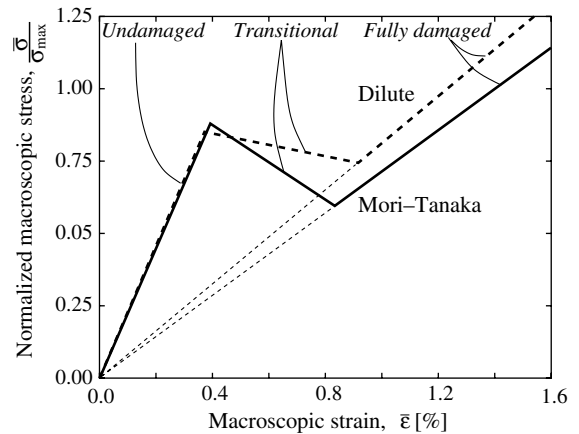


Fig. 3. Comparison between dilute and Mori–Tanaka solutions; $f = 0.2$, $a = 40 \mu\text{m}$.

sponse is trilinear, with the undamaged and fully damaged portions of the curve passing through the origin (as indicated by the dotted lines in Fig. 3). The fully damaged solution, for which all interfaces have debonded (i.e., $\sigma_I^{\text{int}} = 0 \forall I$), corresponds to the response of a linearly elastic material with a void volume fraction f (i.e. porous medium). The sign of the coefficient α'_I defined in (17) determines the slope of the transitional stage of the macroscopic stress–strain curve.

The predicted undamaged response and onset of the transition between undamaged and fully damaged states are, for this value of f , very similar between the dilute and the Mori–Tanaka models. However, as is apparent in Fig. 3 even for this relatively low volume fraction, substantial differences

exist between the two micromechanics models in the transition and fully damaged responses. Since we are primarily interested in composite systems with moderate to high particle volume fractions, we will focus the remainder of this discussion on the Mori–Tanaka model.

The effect of the volume fraction on the $\bar{\sigma}$ – $\bar{\epsilon}$ curve is shown in Fig. 4. As expected, due to the stiffness mismatch between the particles and the matrix, an increasing value of f leads to a stiffening undamaged response and a more compliant fully damaged response. Note that the maximum theoretical packing density of circles of a single size in a plane is $f \approx 0.91$, in contrast to the maximum for spheres, which is $f \approx 0.78$. In practice, the high volume fractions in energetic materials are achieved by using a distribution of particle sizes. When there is more than one particle size, as in Fig. 5, the macroscopic stress–strain curve becomes more complex, with critical points corresponding to damage initiation and complete failure for each of the phases, starting with the larger particles, as observed experimentally.

Fig. 6 shows the effect of the particle radius on the macroscopic stress–strain curve for a fixed volume fraction. Increasing the radius decreases the slope of the transitional stage, which suggests the existence of a critical radius, a_{cr} , below which the composite hardens in the transitional phase, and above which the material softens. Tan et al. (2006, 2005a) differentiate between stable and unstable paths, with catastrophic debonding possible under load control for particles larger than the critical particle size. However, as we will see in Section 5, even the mono-

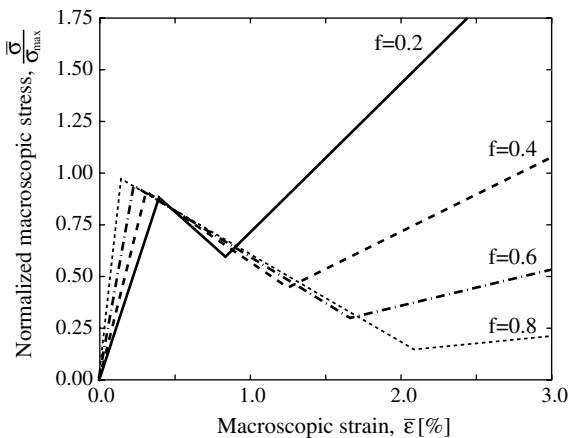


Fig. 4. Effect of volume fraction on the macroscopic stress–strain curve: Mori–Tanaka solution, $a = 40 \mu\text{m}$.

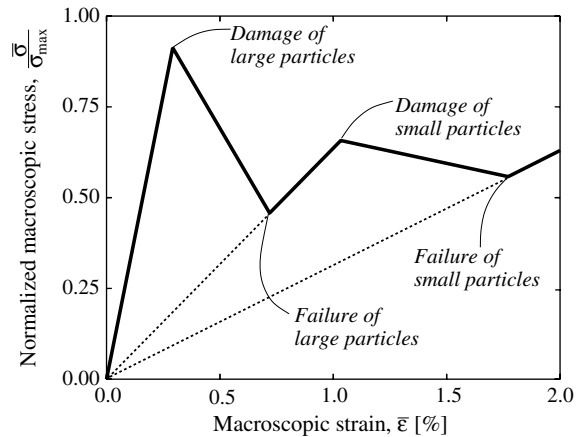


Fig. 5. Macroscopic stress strain-curve for a material with two different particle sizes, $a_1 = 50 \mu\text{m}$, $f_1 = 0.26$, $a_2 = 20 \mu\text{m}$, $f_2 = 0.18$.

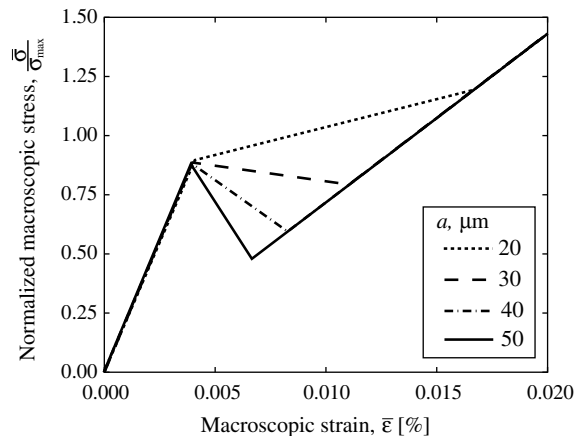


Fig. 6. Effect of particle radius: Mori–Tanaka solution, with volume fraction $f = 0.2$.

tonically increasing macroscopic responses show instability under equibiaxial loading.

4. MTH-based multiscale finite element method

Consider the multiscale structural problem shown in Fig. 7. The macroscopic scale \mathbf{x} is related to the microscopic scale \mathbf{y} through an asymptotic scaling parameter ζ , as $\mathbf{y} = \mathbf{x}/\zeta$. The macroscopic domain Ω with boundary Γ is subject to mixed boundary conditions. Tractions are applied to Γ_t and displacements are imposed on Γ_d , with $\Gamma = \Gamma_t \cup \Gamma_d$. No body forces are considered in this work. The heterogeneous microscopic domain Θ is assumed to be periodic and contains fibers

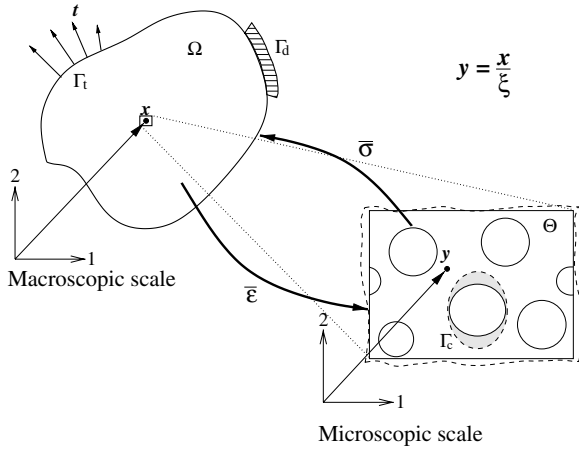


Fig. 7. Multiscale model. The deformed contours drawn on the RVE (dashed curves) emphasize the periodic nature of the microscale solution and the displacement jump along the cohesive fiber–matrix interface.

embedded in a surrounding matrix. The progressive failure of the fiber–matrix interfaces, denoted by Γ_c , is characterized by the cohesive law given in (2)–(4).

We define an asymptotic expansion of the displacement field,

$$\mathbf{u}(\mathbf{x}, \mathbf{y}) \approx \mathbf{u}^{(0)}(\mathbf{x}, \mathbf{y}) + \xi^1 \mathbf{u}^{(1)}(\mathbf{x}, \mathbf{y}) + \xi^2 \mathbf{u}^{(2)}(\mathbf{x}, \mathbf{y}) + \dots, \quad (20)$$

where superscripts in parentheses $^{(0),(1),\dots}$ indicate the asymptotic order. Next, we use the differentiation operator

$$\frac{\partial \phi(\mathbf{x}, \mathbf{y})}{\partial \mathbf{x}} = \frac{\partial \phi}{\partial \mathbf{x}} + \frac{1}{\xi} \frac{\partial \phi}{\partial \mathbf{y}} \quad (21)$$

to derive the asymptotic expansion of the displacement gradient

$$\begin{aligned} \frac{\partial u_i}{\partial x_j} \approx & \frac{\partial u_i^{(0)}}{\partial x_j} + \frac{1}{\xi} \frac{\partial u_i^{(0)}}{\partial y_j} + \xi \frac{\partial u_i^{(1)}}{\partial x_j} + \frac{\partial u_i^{(1)}}{\partial y_j} + \xi^2 \frac{\partial u_i^{(2)}}{\partial x_j} \\ & + \xi \frac{\partial u_i^{(2)}}{\partial y_j} + \dots \end{aligned} \quad (22)$$

The strain, defined to be the symmetric part of the strain operator in the small strain setting, is thus given by

$$\begin{aligned} \varepsilon_{ij} \approx & \xi^{-1} \left(\frac{\partial^S u_i^{(0)}}{\partial y_j} \right) + \xi^0 \left(\frac{\partial^S u_i^{(0)}}{\partial x_j} + \frac{\partial^S u_i^{(1)}}{\partial y_j} \right) \\ & + \xi^1 \left(\frac{\partial^S u_i^{(1)}}{\partial x_j} + \frac{\partial^S u_i^{(2)}}{\partial y_j} \right) + \dots, \end{aligned} \quad (23)$$

$$\approx \xi^{-1} \varepsilon_{ij}^{(-1)} + \xi^0 \varepsilon_{ij}^{(0)} + \xi^1 \varepsilon_{ij}^{(1)} + \dots, \quad (24)$$

where we have introduced the symmetric gradient operator

$$\frac{\partial^S \bullet_i}{\partial x_j} = \frac{1}{2} \left(\frac{\partial \bullet_i}{\partial x_j} + \frac{\partial \bullet_j}{\partial x_i} \right). \quad (25)$$

In terms of the material stiffness tensor, \mathbf{E} , the external tractions applied on Γ_t , \mathbf{t} , and the cohesive tractions present on Γ_c , \mathbf{T} , the principle of virtual work (PVW) for this problem is

$$\int_{\Omega} E_{ijkl} \varepsilon_{kl} \frac{\partial^S v_i}{\partial x_j} d\Omega - \int_{\Gamma_t} t_i v_i dS + \int_{\Gamma_c} T_i \llbracket v_i \rrbracket dS = 0, \quad (26)$$

for all admissible displacements \mathbf{v} satisfying

$$\mathbf{v} \in [H^1]^2, \quad \mathbf{v} = 0 \text{ on } \Gamma_d, \quad (27)$$

where $[H^1]^2$ is the Sobolev space for the 2-D problem. Expanding (26) and grouping by powers of ξ leads to

$$\frac{1}{\xi^2} \int_{\Omega} E_{ijkl} \frac{\partial^S u_k^{(0)}}{\partial y_l} \frac{\partial^S v_i}{\partial y_j} d\Omega = 0, \quad (28)$$

$$\begin{aligned} \frac{1}{\xi} \int_{\Omega} E_{ijkl} \left[\left(\frac{\partial^S u_k^{(0)}}{\partial x_l} + \frac{\partial^S u_k^{(1)}}{\partial y_l} \right) \frac{\partial^S v_i}{\partial y_j} + \frac{\partial^S u_k^{(0)}}{\partial y_l} \frac{\partial^S v_i}{\partial x_j} \right] d\Omega \\ + \int_{\Gamma_c} T_i \llbracket v_i \rrbracket dS = 0, \end{aligned} \quad (29)$$

$$\begin{aligned} \int_{\Omega} E_{ijkl} \left[\left(\frac{\partial^S u_k^{(1)}}{\partial x_l} + \frac{\partial^S u_k^{(2)}}{\partial y_l} \right) \frac{\partial^S v_i}{\partial y_j} + \left(\frac{\partial^S u_k^{(0)}}{\partial x_l} + \frac{\partial^S u_k^{(1)}}{\partial y_l} \right) \frac{\partial^S v_i}{\partial x_j} \right] d\Omega \\ = \int_{\Gamma_t} t_i v_i dS. \end{aligned} \quad (30)$$

We make use of the integration operators for y -periodic functions

$$\lim_{\xi \rightarrow 0^+} \int_{\Omega} \phi(\mathbf{x}, \mathbf{y}) d\Omega = \frac{1}{|\Theta|} \int_{\Omega} \int_{\Theta} \phi(\mathbf{y}) d\Theta d\Omega, \quad (31)$$

$$\lim_{\xi \rightarrow 0^+} \xi \int_{\Gamma} \phi(\mathbf{x}, \mathbf{y}) dA = \frac{1}{|\Theta|} \int_{\Omega} \int_{\partial\Theta} \phi(\mathbf{y}) dA_{\Theta} d\Omega, \quad (32)$$

in evaluating (28) and (29). Eq. (30) represents equilibrium at the macroscale and is used to fully couple the macro- and microscale solutions. However, this relation is not used in this work, as we assume a macroscopic strain history $\bar{\varepsilon}$ and extract from the periodic RVE the effect of the microscale damage evolution on the macroscopic stress $\bar{\sigma}$.

As described in detail by Guedes and Kikuchi (1990), from (28) we establish that $\mathbf{u}^{(0)}$ depends only on the macroscale,

$$\mathbf{u}^{(0)}(\mathbf{x}, \mathbf{y}) = \mathbf{u}^{(0)}(\mathbf{x}) \quad (33)$$

with no \mathbf{y} -dependence, and is hence a continuous field. From (33) and (29), we obtain an expression of equilibrium at the microscale

$$\frac{1}{|\Theta|} \int_{\Theta} E_{ijkl} \left[\left(\frac{\partial^S u_k^{(0)}(\mathbf{x})}{\partial x_l} + \frac{\partial^S u_k^{(1)}}{\partial y_l} \right) \frac{\partial^S v_i}{\partial y_j} \right] d\Theta + \frac{1}{|\Theta|} \int_{\Gamma_c} T_i[[v_i]] dS = 0, \tag{34}$$

for all admissible displacements \mathbf{v} satisfying

$$\mathbf{v} \in [H^1]^2, \quad \mathbf{v}(\mathbf{y}) \text{ is } Y\text{-periodic on } \partial\Theta. \tag{35}$$

Defining the macroscopic strain, $\bar{\boldsymbol{\varepsilon}} = \frac{\partial^S \mathbf{u}^{(0)}}{\partial \mathbf{x}}$, and the fluctuating strain, $\tilde{\boldsymbol{\varepsilon}} = \frac{\partial^S \mathbf{u}^{(1)}}{\partial \mathbf{y}}$, and considering the macroscopic strain as having the effect of a loading term at the microscale, we can rearrange (34) in the following form:

$$\frac{1}{|\Theta|} \int_{\Theta} E_{ijkl} \tilde{\varepsilon}_{kl} \frac{\partial^S v_i(\mathbf{y})}{\partial y_j} d\Theta + \frac{1}{|\Theta|} \int_{\Gamma_c} T_i[[v_i]] dS = -\frac{1}{|\Theta|} \int_{\Theta} E_{ijkl} \frac{\partial^S v_i(\mathbf{y})}{\partial y_j} d\Theta \bar{\varepsilon}_{kl}, \tag{36}$$

which serves as the basis for the finite element solution for the discontinuous displacement field $\mathbf{u}^{(1)}$. In the following, we refer to $\mathbf{u}^{(0)}$ as the *macroscopic* dis-

placement, and $\mathbf{u}^{(1)}$ as the *fluctuating* displacement. The macroscopic stress $\bar{\boldsymbol{\sigma}}$ is given by the volume average of the local stress field. Note that the macroscopic stress and strain defined in this section have the same meaning as those defined in Section 3.

A sample representative volume element (RVE) of a simulated particulate composite containing 50 circular particles is shown in Fig. 8(a). The RVE is square, with edges of length 693.5 μm . The particle radius distribution is bimodal, as shown in Fig. 8(b), with peaks at $a = 50$ and 30 μm , and with volume fractions of 0.26 and 0.18, respectively. The total particle volume fraction is thus 0.44. The particles and matrix are discretized with 3- and 4-noded elements using the T3D meshing tool (Rypl and Bittnar, 2002), which creates a periodic mesh. The particle–matrix interfaces are modeled with 4-noded cohesive elements. To enforce periodicity, corresponding nodes on opposite edges are assigned the same equation number. The nonlinear system of equations resulting from (36) is solved using the stiffness matrix from the previous load step, with

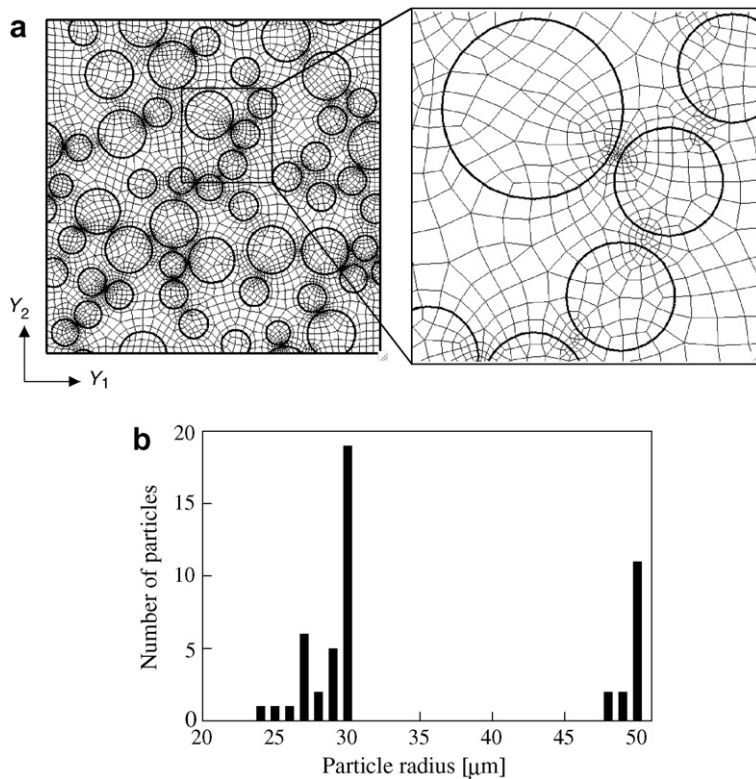


Fig. 8. (a) Typical RVE mesh, incorporating 3- and 4-noded elements, with refinement in areas of high heterogeneity. (b) Particle size distribution.

an adaptive load stepping scheme to ensure accuracy and efficiency of computational effort. The mesh is checked to ensure that there are sufficient cohesive elements within the cohesive zone. More details on the packing and discretization methodologies can be found in Matouš et al. (2006).

Fig. 9 shows results from this RVE under an imposed macroscopic equibiaxial strain, $\bar{\epsilon} = (\bar{\epsilon}_{11}, \bar{\epsilon}_{22}, \bar{\epsilon}_{12}) = (0.0045, 0.0045, 0.0000)$. The macroscopic stress–strain (left axis) and cohesive damage evolution (right axis) are plotted on the same graph to allow for a direct correlation between microscale damage and macroscopic constitutive response. The macroscopic stresses $\bar{\sigma}_{11}$ and $\bar{\sigma}_{22}$ are normalized

by the critical opening stress σ_{\max} . Below the graph, a sequence of von Mises stress fields, σ_{vm} , are plotted on the deformed shape, with displacements magnified 10 times. The gray scale maps have been normalized and the range limited to allow clear discernment of variations in the fields. For this reason, the signal saturates in regions of particularly high stresses.

The dash-dotted curve corresponds to the evolution of the fraction of cohesive elements which are damaged, i.e., those which are in the downward portion of the cohesive curve in Fig. 1, while the dashed and dotted curves denote the fraction of fully failed cohesive elements on the boundaries of large and

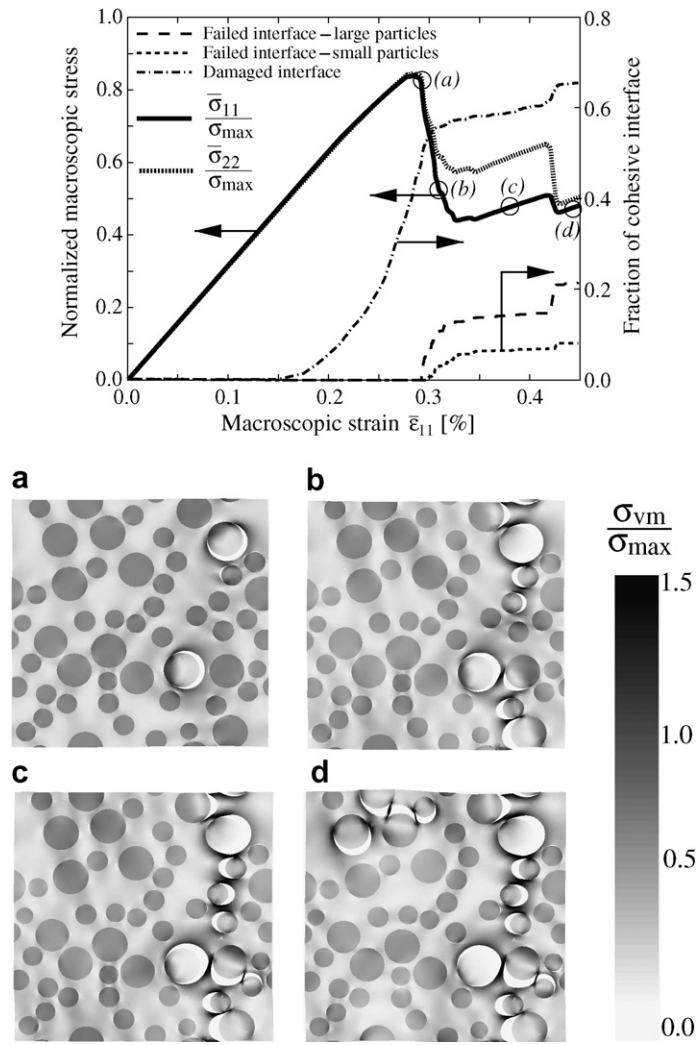


Fig. 9. (Top) MTH prediction of macroscopic stress–strain and damage evolution curves for equibiaxial strain case. (Bottom) Von Mises stress distributions plotted on the deformed shape (displacements magnified by 10) of the RVE at the four stages in the damage process denoted by open circles in the top figure.

small particles, respectively. As apparent in Fig. 9, a substantial fraction (about 40%) of the particle–matrix interfaces is damaged before we can discern a deviation from linearity in the stress–strain curves. Under the highly unstable macroscopic equibiaxial strain, the damage evolution curve rises rapidly up to the point at which the first interfaces fail completely leading to a sudden dropoff in macroscopic stresses, as indicated by (a). Failure commences at the large particles and in regions of locally high volume fraction and is a sudden event. The initial interfacial failure drives a localization process, visible in (b), resulting in a loss of stress equibiaxiality, with $\bar{\sigma}_{11} < \bar{\sigma}_{22}$ since the system becomes more compliant in the direction normal to the localization band. Localization continues until all the particles across the height of the RVE have failed, at (c). At this

point, we note that, in reality, the small remaining ligaments of matrix between the decohered particles would tear, causing complete failure of the component. However, since matrix tearing is not considered in this study, continuing loading causes a new process of localization to initiate perpendicular to the original localization direction, as shown in (d), resulting in a return to near equibiaxiality of the macroscopic stresses. Throughout this sequence, the periodicity of the domain is evident, with displacements and stresses at opposite boundaries of the RVE being identical. Failure occurs preferentially at the interfaces of large particles, in agreement with experimental observations.

Fig. 10 presents the macro- and micro-scale results associated with $\bar{\epsilon} = (0.006, 0, 0)$. The uniaxial state of macroscopic strain leads to a more stable

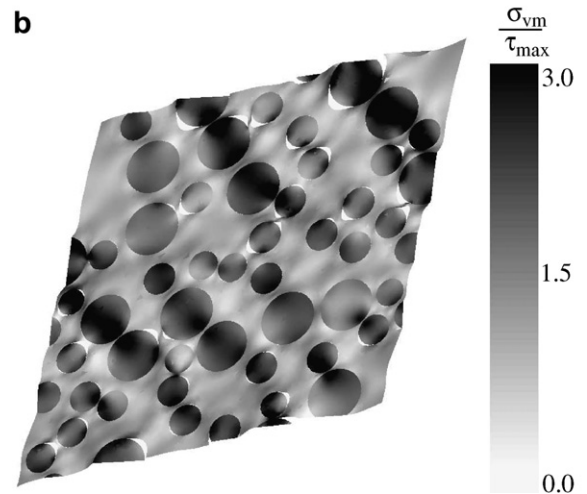
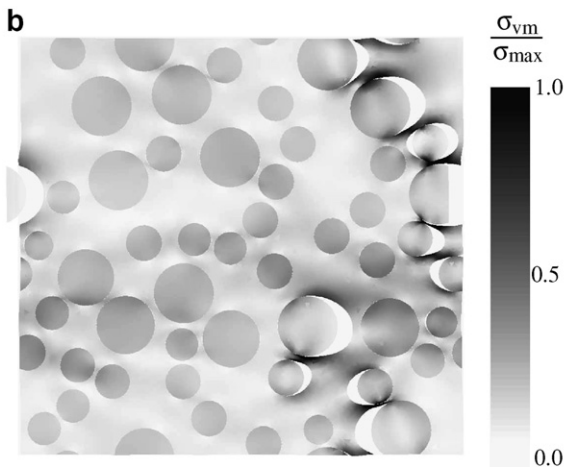
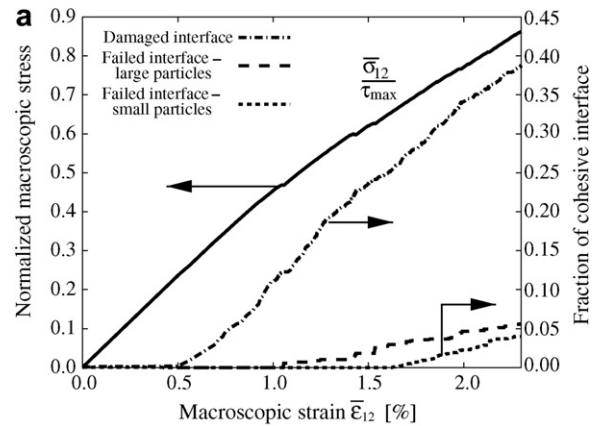
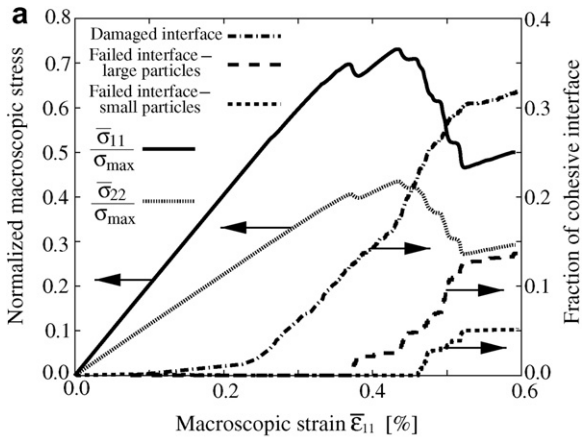


Fig. 10. Uniaxial macroscopic strain: (a) Macroscopic stress–strain curve, including damage evolution; (b) Von Mises stress distribution at $\bar{\epsilon}_{11} = 0.6\%$. The displacements have been magnified by 10 to emphasize the interface failure.

Fig. 11. Macroscopic shear stress state: (a) Macroscopic stress–strain curve, including damage evolution; (b) Von Mises stress distribution at $\bar{\epsilon}_{11} = 2.3\%$. Displacements magnified by 10.

macroscopic solution. In this case, failure initiates at large particles, with opening normal to the applied loading direction. Due to the lower level of stress biaxiality, the failure process is less sudden, although localization of damage still appears in the direction perpendicular to the applied macroscopic strain. Note the presence of stress concentrations in the vicinity of interfacial crack tips.

The solution is quite different in the shear loading case (Fig. 11), for a macroscopic strain of $\bar{\epsilon} = (0, 0, 0.023)$. The maximum principal stress is at a 45° angle to the RVE axes, and the openings are again normal to the applied load. The large negative principal stress results in considerably less failure of the cohesive interfaces than in the two other loading cases, and prevents crack propagation along the interfaces. Instead of the damage localization observed in the other two loading cases, we observe much more distributed damage in the RVE, which leads to a very limited deviation from linearity in the macroscopic $\bar{\sigma}_{12}-\bar{\epsilon}_{12}$ curve (Fig. 11(a)). As in the uniaxial strain case, damage initiates around the larger particles. Some of the cohesive failure is in rotation, particularly evident in those particles which are on the periodic boundaries.

5. Comparative assessment

In order to compare the micromechanics and MTH-based finite element (MTHFE) models, we consider first a single particle unit cell subjected to equibiaxial loading. Periodic boundary conditions impose a regular stacking of unit cells, thus the single particle cell represents a regular array of parti-

cles. The volume fraction can be easily controlled by changing the size of the unit cell while keeping the particle size constant. Fig. 12 shows the results of this comparison for low volume fraction ($f = 0.2$) for particles smaller (a) and larger (b) than the aforementioned critical particle size, $a_{cr} = 27 \mu\text{m}$ for this material system. In all the comparative curves, dashed lines represent the micromechanics prediction, and solid curves are used for the results of the MTHFE simulation.

As apparent in Fig. 12 the Mori–Tanaka solution captures the essential features of the MTHFE result, with the initial slope and damage initiation point in good agreement between the two, and the final slope of the MTHFE tending toward that predicted by the Mori–Tanaka model. However, the two solutions differ substantially in the transition phase. Although the MTHFE curve initially follows the slope of the micromechanics prediction, there is an instability present in the solution regardless of whether the predicted material response is monotonic or not. This instability can be related to variations in stress concentration around the particle boundary, a consequence of the periodic arrangement of particles, where points at the top, bottom, left and right of the particle are the closest to a neighboring particle. Slight differences in cohesive tractions experienced at different points of the particle–matrix interfaces, coupled with randomness in the mesh (analogous to randomness in the particle shape or local variations in material properties in a real material) cause the problem to lose axisymmetry. The instability of the loading conditions and the softening cohesive law create a path which drives

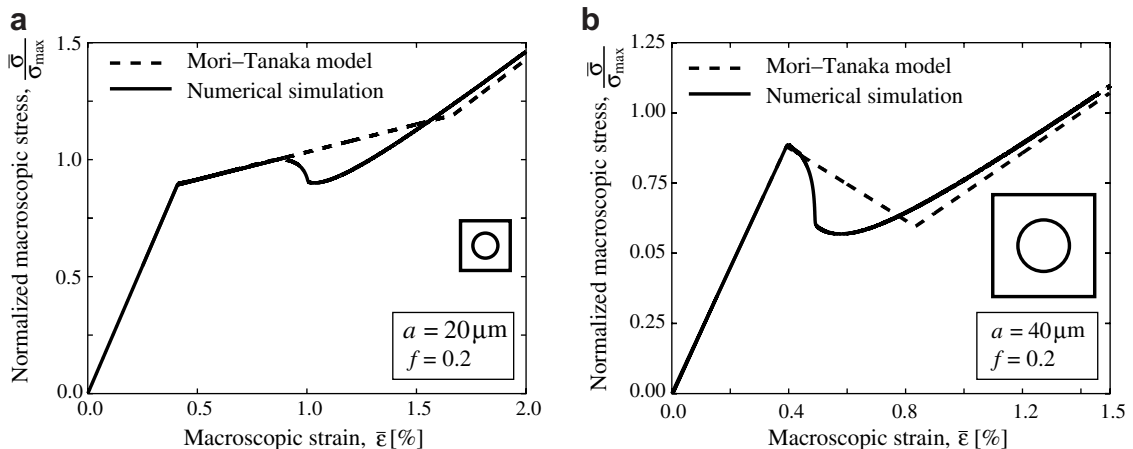


Fig. 12. Comparison between micromechanics and MTH solutions (a) $a < a_{cr}$, (b) $a > a_{cr}$.

rapid failure of the portion of the interface which was initially perturbed. We see that, while the Mori–Tanaka solution assumes that failure occurs axisymmetrically and uniformly, MTHFE allows failure to occur non-uniformly, through crack initiation at a random location, followed by crack propagation around the interface. The interface never fails completely, hence the final slope of the MTHFE solution does not decline to that predicted by micromechanics. Once a considerable portion of the interface has failed, little driving force remains to debond the last few elements.

To investigate the effect of non-regular particle distribution, we perform the same comparison on a periodic unit cell containing 18 particles in a random array, shown in Fig. 13. (This locally random particle arrangement is, however, repeated through periodicity.) For reference, the solution for a single

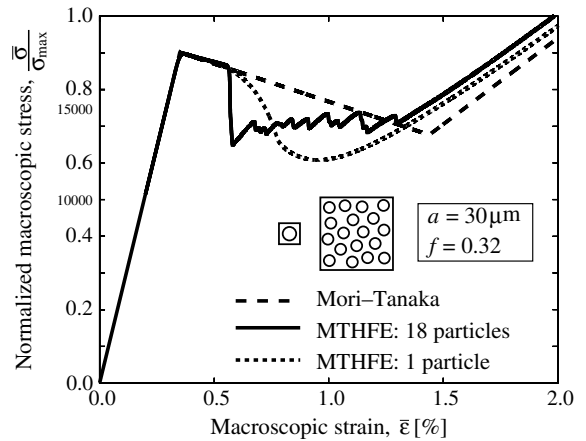


Fig. 13. Comparison between micromechanics and MTH solutions for a unit cell containing 18 particles. The failure of each particle is a discrete event.

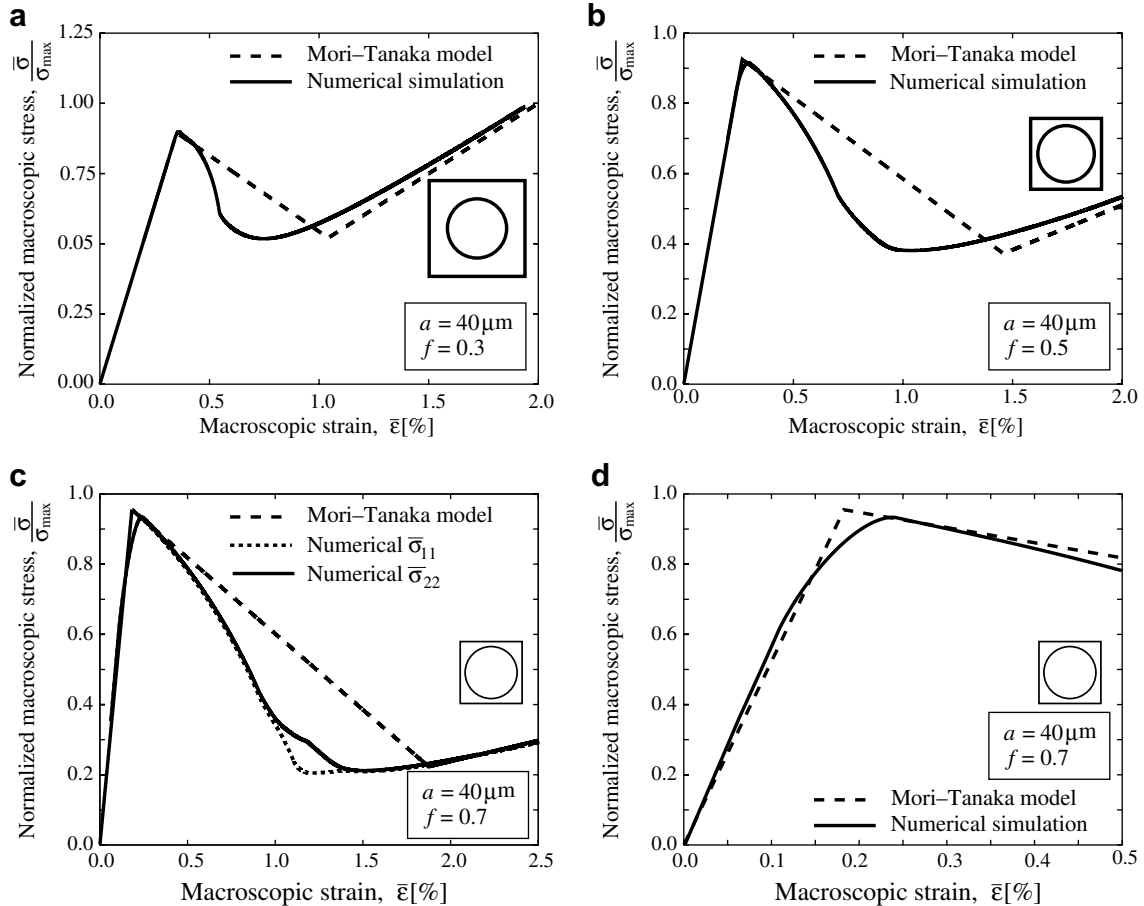


Fig. 14. Comparison between micromechanics and MTH solutions for $a = 40 \mu\text{m}$, with varying volume fraction: (a) $f = 0.3$, (b) $f = 0.5$, (c) $f = 0.7$, (d) is a magnification of the first part of the curve in (c).

particle with the same volume fraction and particle size is plotted on the same graph, with a dotted curve. While the beginning of instability occurs at almost the same point for both simulations, the dropoff is much more sudden for the multi-particle system than it is for a single particle, due to particle interaction and localization. As failure initiates in one particle, that drives failure for all the particles across the height or width of the cell. The failure process is discrete, as an ongoing failure process relieves stresses elsewhere in the RVE, delaying the failure of other particles.

Thus far, we have considered only microstructures with low volume fractions. Fig. 14 shows results for volume fractions as high as $f = 0.7$ (close to the maximum possible for a rectangular array). As seen earlier, for low volume fraction, the models are in good agreement about key features of the solution. As the volume fraction increases, the level of agreement between the two models in the transition region decreases. The difference is particularly obvious in Fig. 14(c) and (d). This is expected since the Mori–Tanaka assumption is known to be valid only for low to moderate volume fractions. The Mori–Tanaka model also underpredicts the initial slope slightly. The sharp damage initiation point, a consequence of the bilinear cohesive law, is present in the solutions at low volume fraction, but becomes less marked as f increases. The increasing packing density results in an increase in stress concentration at localized points on the particle boundary, causing damage to begin earlier than predicted. The transitional phase does not display the same sudden dropoff as observed for lower volume fraction and the slope is significantly more negative in the entire region, since failure is not occurring at the same rate everywhere around the boundary.

Real material systems have multiple particle sizes. Fig. 15 shows the results of a simulation with two different particle sizes. For particles of similar sizes, shown in (a), stress concentrations and localization processes play a significant role. The failure processes for large and small particles are not independent, as predicted by the micromechanics solution. However, once the difference between particle sizes becomes significant, as in (b), the effect of the smaller particles on the failure process is reduced substantially. The smaller particles serve merely to stiffen the binder and to trigger damage nucleation through local stress concentration. This is evident in both the MTHFE and micromechanics results,

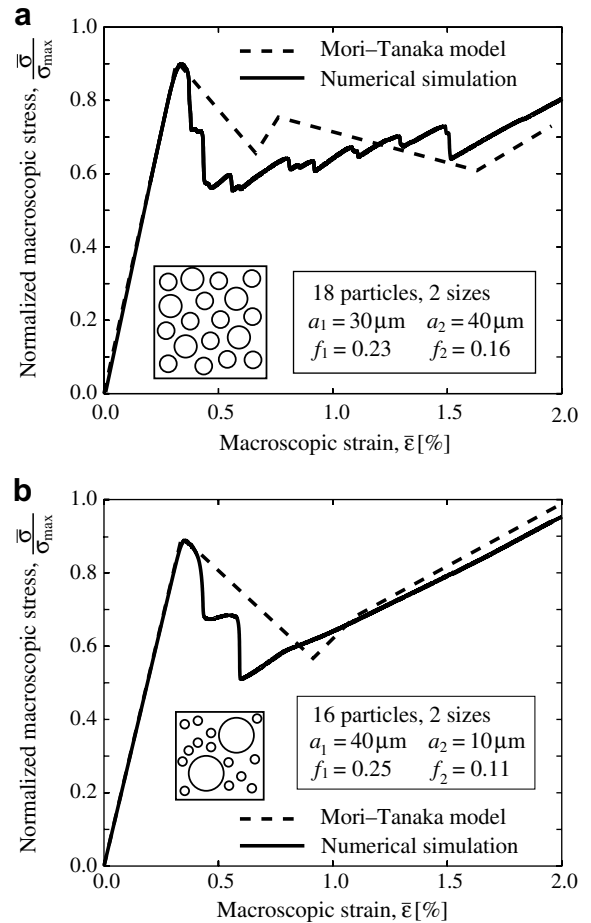


Fig. 15. Comparison between micromechanics and MTH solutions for two different particle sizes: (a) shows a system in which the particles are of the same order of magnitude. In (b) the difference in size is more marked. The small particles have not yet failed at $\bar{\epsilon} = 0.02$, hence the MTHFE is still below the Mori–Tanaka prediction.

indicating that the micromechanics model, while not fully capturing the failure process, can nonetheless give useful information about which particles need to be modeled.

6. Conclusions

We have performed a detailed comparative assessment of micromechanics and finite element based homogenization schemes for the problem of debonding damage in a plane strain particulate composite system. Special emphasis has been placed on the ability of the two schemes to capture particle-to-particle interactions and the effect of dissimilar particle sizes.

The plane strain micromechanics model developed by Tan et al. (2005a) is effective at capturing key features of the macroscopic stress–strain response for minimal computational effort. The shortcomings of this model are that it cannot capture the instability inherent in the system or the heterogeneous stress and strain fields. In a highly filled composite, interactions between particles are a significant contributor to failure through local stress concentrations and the occurrence of localization. The micromechanics model does not capture these interactions during the failure process, and hence ceases to be predictive under high volume fraction, $f > 0.5$, when stress concentrations begin to play a significant role in the solution, or when the particle distribution is random, resulting in localization. Both models demonstrate that, for large differences in particle diameters, it is unnecessary to model the debonding of smaller particles, but it is sufficient to represent their contribution to damage nucleation and to the stiffness of the matrix.

The ability of the MTHFE code to function as a direct numerical simulation for validation of simpler models has been demonstrated. The MTH-based code has an ability to capture a richness of details about the physical response of the system. The method is capable of solving more complex loading cases, and can be extended to include different material models and nonlinear kinematics, which is of particular interest in the modeling of damage in energetic materials.

Acknowledgements

This work was supported by the Center for Simulation of Advanced Rockets (CSAR) under Contract number B341494 by the US Department of Energy. K. Matouš and P.H. Geubelle also acknowledge support from ATK/Thiokol (Program Managers, J. Thompson and Dr. I. L. Davis). H. Tan and Y. Huang acknowledge additional support from ONR Composites for Marine Structures Program (Grant N00014-01-1-0205, Program Manager Dr. Y.D.S. Rajapakse).

References

- Bencher, C.D., Dauskardt, R.H., Ritchie, R.O., 1995. Microstructural damage and fracture processes in a composite solid rocket propellant. *Journal of Spacecraft and Rockets* 32 (2), 328–334.
- Bensoussan, A., Lions, J.L., Papanicolaou, G., 1978. *Asymptotic Analysis for Periodic Structures*. North-Holland.
- Benveniste, Y., Aboudi, J., 1984. A continuum model for fiber reinforced materials with debonding. *International Journal of Solids and Structures* 20, 935–951.
- Budiansky, B., 1965. On the elastic moduli of some heterogeneous materials. *Journal of the Mechanics and Physics of Solids* 13, 223–227.
- Eshelby, J.D., 1957. The determination of the elastic field of an ellipsoidal inclusion, and related problems. *Proceedings of the Royal Society of London A* 241, 376–396.
- Fish, J., Shek, K., Pandheeradi, M., Shephard, M.S., 1997. Computational plasticity for composite structures based on mathematical homogenization: theory and practice. *Computer Methods in Applied Mechanics and Engineering* 148, 53–73.
- Geubelle, P.H., Baylor, J.S., 1998. Impact-induced delamination of composites: a 2D simulation. *Composites Part B* 29B, 589–602.
- Ghosh, S., Lee, K., Moorthy, S., 1995. Multiple scale analysis of heterogeneous elastic structures using homogenization theory and Voronoi cell finite element method. *International Journal of Solids and Structures* 32 (1), 27–62.
- Guedes, J.M., Kikuchi, N., 1990. Preprocessing and postprocessing for materials based on the homogenization method with adaptive finite element methods. *Computer Methods in Applied Mechanics and Engineering* 83, 143–198.
- Hashin, Z., Shtrikman, S., 1962. A variational approach to the theory of the elastic behaviour of polycrystals. *Journal of the Mechanics and Physics of Solids*.
- Hill, R., 1965. A self-consistent mechanics of composite materials. *Journal of the Mechanics and Physics of Solids* 13, 213–222.
- Ide, K.M., Ho, S.-Y., 1999. Fracture behaviour of accelerated aged solid rocket propellants. *Journal of Materials Science* 34, 4209–4218.
- Kanit, T., Forest, S., Galliet, I., Mounoury, V., Jeulin, D., 2003. Determination of the size of the representative volume element for random composites: statistical and numerical approach. *International Journal of Solids and Structures* 40, 3647–3679.
- Matouš, K., Geubelle, P., 2006. Multiscale modeling of particle debonding in reinforced elastomers subjected to finite deformations. *International Journal for Numerical Methods in Engineering* 65, 190–223.
- Matouš, K., Inglis, H.M., Gu, X., Rypl, D., Jackson, T.L., Geubelle, P.H., 2006. Multiscale modeling of solid propellants: From particle packing to grain failure. *Composites Science and Technology*, doi:10.1016/j.compscitech.2006.06.017.
- Mori, T., Tanaka, K., 1973. Average stress in matrix and average elastic energy of materials with misfitting inclusions. *Acta Metallurgica* 21, 571–574.
- Rae, P.J., Goldrein, H.T., Palmer, S.J.P., Field, J.E., Lewis, A.L., 2002a. Quasi-static studies of the deformation and failure of β -HMX based polymer bonded explosives. *Proceedings of the Royal Society of London A* 458, 743–762.
- Rae, P.J., Palmer, S.J.P., Goldrein, H.T., Field, J.E., Lewis, A.L., 2002b. Quasi-static studies of the deformation and failure of PBX 9501. *Proceedings of the Royal Society of London A* 458, 2227–2242.
- Raghavan, P., Moorthy, S., Ghosh, S., Pagano, N., 2001. Revisiting the composite laminate problem with an adaptive multi-level computational model. *Composites Science and Technology* 61, 1017–1040.

- Rypl, D., Bittnar, Z., 2002. Hybrid method for generation of quadrilateral meshes. *Engineering Mechanics* 9, 49–64.
- Sanchez-Palencia, E., 1980. *Non-Homogeneous Media and Vibration Theory*. Lecture Notes in Physics No. 127. Springer-Verlag.
- Tan, H., Huang, Y., Liu, C., Geubelle, P.H., 2005a. The Mori–Tanaka method for composite materials with nonlinear interface debonding. *International Journal of Plasticity* 21, 1890–1918.
- Tan, H., Liu, C., Huang, Y., Geubelle, P.H., 2005b. The cohesive law for the particle/matrix interfaces in high explosives. *Journal of the Mechanics and Physics of Solids* 53, 1892–1917.
- Tan, H., Huang, Y., Liu, C., Geubelle, P.H., 2006. The effect of nonlinear interface debonding on the constitutive model of composite materials. *International Journal for Multiscale Computational Engineering* 4, 147–167.
- Timoshenko, S.P., Goodier, J.N., 1970. *Theory of Elasticity*, Third ed. McGraw-Hill.
- Trumel, H., Dragon, A., Fanget, A., Lambert, P., 2001. A constitutive model for the dynamic and high-pressure behaviour of a propellant-like material: Part I: Experimental background and general structure of the model. *International Journal for Numerical and Analytical Methods in Geomechanics* 25, 551–579.